An experimental study on crack propagation at rock-concrete interface using digital image correlation technique

Wei Dong[1,*], Zhimin Wu[2], Xiangming Zhou[3], Na Wang[4], Gediminas Kastiukas[5]

[1]Associate Professor, State Key Laboratory of Coastal and Offshore Engineering, Dalian University of Technology, Dalian 116024, P. R. China.

(*Corresponding author). E-mail: dongwei@dlut.edu.cn

[2]Professor, State Key Laboratory of Coastal and Offshore Engineering, Dalian University of Technology, Dalian 116024, P. R. China. E-mail: wuzhimin@dlut.edu.cn

[3]Reader in Civil Engineering Design, Department of Mechanical, Aerospace and Civil Engineering, Brunel University London, Uxbridge, Middlesex UB8 3PH, UK & Haitian Visiting Professor, State Key Laboratory of Coastal and Offshore Engineering, Dalian University of Technology, Dalian 116024, P. R. China. E-mail: xiangming.zhou@brunel.ac.uk

[4]Master student, State Key Laboratory of Coastal and Offshore Engineering, Dalian University of Technology, Dalian 116024, P. R. China. E-mail: wangna@163.com

[5]PhD student, Department of Mechanical, Aerospace and Civil Engineering, Brunel University London, Uxbridge, Middlesex UB8 3PH, UK. E-mail: Gediminas.Kastiukas@brunel.ac.uk

ABSTRACT

The digital image correlation (DIC) technique is employed to investigate the fracture process at rock-concrete interfaces under three-point bending (TPB), and four-point shearing (FPS) of rock-concrete composite beams with various pre-crack positions. According to the displacement fields obtained from experiment, the crack width, and propagation length

during the fracture process can be derived, providing information on the evolution of the fracture process zone (FPZ) at the interface. The results indicated that under TPB, the fracture of the rock-concrete interface is mode I dominated fracture although slight sliding displacement was also observed. Under FPS, the mode II component may increase in the case of a small notched crack length-to-depth ratio, resulting in the crack kinking into the rock. It was also observed that the FPZ length at the peak load is far longer for a specimen under FPS than under TPB.

Keywords: Rock-concrete interface; digital image correlation; fracture process zone; crack propagation; fracture mode

1. Introduction

For concrete structures built on a rock foundation, e.g. concrete dams, the interface between concrete and rock is usually considered as the weakest structural zone, enabling cracks to initiate and propagate along the interface under the hydrostatic loading. Similar to cement-based materials, a rock-concrete interface exhibits a typical quasi-brittle behaviour, i.e. there is a fracture process zone (FPZ) ahead of the interfacial crack, which features strain softening and strain localization behavior. Both the FPZ length and the crack opening displacement in the FPZ are essential parameters for characterizing the nonlinear behavior of concrete. Considering the small size of the FPZ compared with the large size of structures, some researchers [1, 2] have employed linear elastic fracture mechanics to analyze the fracture behavior of rock-concrete interfaces, in which the FPZ length was ignored. However,

based on the linear elastic fracture mechanics, once a crack initiates, it will immediately enter the unstable propagation stage, i.e. the nonlinear response of a structure cannot be reflected without an FPZ. Meanwhile, it is well known that fracture energy plays an important role in the fracture analysis of cementitious materials [3] and is significantly affected by the size of the FPZ [4]. By comparing the linear and nonlinear fracture methods (with/without FPZ), Červenka et al. [5] demonstrated that performing a nonlinear analysis of a cementitious material interface could increase the critical fracture energy by approximately 20% compared to a linear analysis. Therefore, with regards to the safety assessment of rock-concrete structures such as concrete dams built on a rock foundation, nonlinear fracture mechanics is more reliable for fracture analysis of a rock-concrete interface in the field.

So far, both experimental and numerical methods have been utilized to study FPZ evolution in quasi-brittle materials. Some studies have shown that the FPZ length of concrete decreases rapidly when a crack approaches the top surface of a specimen [6-8]. This is often called the boundary effect and has been successfully explained through the concept of local fracture energy [6, 9, 10]. Based on the experimental results of mode I fracture, it was found that the maximum FPZ length of concrete increases with the increase of the specimen height, and decreases with the increase of the notched crack length-to-depth ratio (a_0/D) [11]. Dong et al. arrived to the same conclusion [12] by introducing the initial fracture toughness criterion in the analysis of concrete fracture. It has also been found in this study, that the FPZ length may continue increasing even after the FPZ has fully developed. Meanwhile, taking sandstone as an example, the FPZ evolution under mixed mode fracture was studied

through experiment [13]. It should be noted that the aforementioned studies aimed at investigating the FPZ evolution in single materials, such as concrete and sandstone. In the case of a composite material such as a rock-concrete interface, to the best of the authors' knowledge, no study regarding its FPZ evolution has been reported. In the few studies which have been made on crack propagation along a rock-concrete interface [14-16], the main objective was to develop a numerical method to effectively simulate the fracture process at the interface rather than to investigate crack evolution. In those studies, usually the curves of load vs. crack mouth opening and sliding displacements (P-CMOD, P-CMSD) obtained from experiment were compared with the ones from simulation to verify the proposed numerical methods. In fact, for the purpose of an in-depth insight into a fracture mechanism, the verification of a numerical method using the FPZ evolution in various fracture stages is more significant and convincing. Therefore, together with the fracture behavior, it is important to investigate the FPZ evolution at the rock-concrete interface.

Digital image correlation (DIC) is an optical technique that is used to visualize the surface displacements of a specimen. Through a comparison of digital images of specimen surfaces before/after deformation, the displacements of the regular grid points on the specimen surface can be obtained, so that the FPZ evolution during fracture process can be derived if combined with a softening constitutive law for crack opening displacement and cohesive force. Due to its convenience, high responsiveness, accuracy and non-destructive nature, the DIC technique has been widely used for investigating a number of processes, including the fracture and fatigue behavior of strengthened reinforced concrete beams [17], the mode I fracture in cementitious materials [11, 18-20], the mixed mode fracture in sandstone [13], the

fracture properties at concrete-concrete interfaces [21], and the interfacial debonding properties in concrete [22]. The results of the above research have demonstrated that the DIC technique can be used to carry out the fracture analysis of concrete with reasonable accuracy.

In this study, the DIC technique is employed to investigate the fracture properties and characterize the FPZ length under three-point bending (TPB) for the rock-concrete interface. Also, in the case of four-point shearing (FPS), the crack opening and sliding displacements at various stages before the peak loads are obtained using the DIC technique with respect to different mode mixity ratios. Based on the experimental results, the FPZ evolution during crack propagation and the effects of the mode mixity ratio on fracture properties are discussed. It is expected that the experimental results presented here can lead to a better understanding of the fracture properties and failure characteristics of rock-concrete interfaces so that the nonlinear fracture mechanics can be more efficiently employed to crack propagation analysis. Meanwhile, it may be helpful to verify the previously developed numerical method for simulating the fracture process of different material interfaces by providing experimental evidence of the FPZ evolution and crack opening/sliding displacements.

2. Experimental Program

2.1 Specimen Preparation and Experimental Setup

The two types of specimens tested in this study were 100 × 100 × 500 mm (width×depth×length) beams with a 400 mm span. One specimen featured an interfacial

notch at the geometric center of the composite, i.e. both the concrete and rock blocks have the same length, for the TPB test (See Fig. 1(a)). The other specimen featured an eccentric interfacial notch, i.e. the concrete and rock blocks have unequal lengths, for FPS test (See Fig. 1(b)). Here, a_0 is the initial crack length; *D, B, and L* are the depth, width and length of the beams, respectively; L_1, L_2, and C_1 are the distances from the two loading points and pre-notch to the geometric center of the rock-concrete composite specimens, respectively. The specimen number "TPB 30" denotes a TPB beam with a_0=30 mm. The specimen number "FPS10-5-60" denotes an FPS beam with L_1/L_2=10, C_1=5 mm, and a_0=60 mm. To obtain the various mode mixty ratios, i.e. K_1/K_2, in the interfacial fracture, the values of a_0, L_1/L_2, and C_1 vary, which are listed in Table 2. Here, K_1 and K_2 are the stress intensity factors of the bi-material interface crack. In this paper, SIFs for a rock-concrete interface crack are calculated by the displacement extrapolation method [23] using the ANSYS finite element code with the formulas shown as below:

$$K_1 = C\lim_{r\to 0}\sqrt{\frac{2\pi}{r}}\left[\delta_y(\cos Q + 2\varepsilon\sin Q) + \delta_x(\sin Q - 2\varepsilon\cos Q\right] \tag{1}$$

$$K_2 = C\lim_{r\to 0}\sqrt{\frac{2\pi}{r}}\left[\delta_y(\cos Q + 2\varepsilon\sin Q) - \delta_x(\sin Q - 2\varepsilon\cos Q\right] \tag{2}$$

where,

$$C = \frac{2\cosh(\varepsilon\pi)}{(\kappa_1+1)/\mu_1 + (\kappa_2+1)/\mu_2} \tag{3}$$

$$Q = \varepsilon\ln r \tag{4}$$

$$\varepsilon = \frac{1}{2\pi}\ln\left(\frac{\frac{\kappa_1}{\mu_1}+\frac{1}{\mu_2}}{\frac{\kappa_2}{\mu_2}+\frac{1}{\mu_1}}\right) \tag{5}$$

$$\mu_i = \frac{E_i}{2(1+v_i)} \qquad (i = 1,2) \tag{6}$$

$$\kappa_i = \begin{cases} (3 - n_{ui}) / (1 + n_{ui}) & \text{(Plane stress)} \\ (3 - 4n_{ui}) & \text{(Plane strain)} \end{cases} \tag{7}$$

E and n_u are the Young's modulus and Poisson's ratio, respectively, while i=1, 2 representing concrete and rock respectively.

To obtain the natural surface of the rock, TPB test was carried out on rock beams with a notch. Once a notched rock beam is broken into two halves under bending, each half will have a natural surface. Mix proportions of the concrete for this study were 1:0.62:1.8:4.2 (cement: water: sand: aggregate) by weight and the maximum aggregate size was 10 mm. To make rock-concrete composite beams, a rock block was placed inside the mould and concrete was cast against it. After curing in sealed conditions for 2 days, the composite specimens were de-moulded and moved into a curing room with 23°C and 90% RH for further curing to 28 days. The measured material properties of concrete, rock, and rock-concrete interface are listed in Table 2, in which E_t, n_u, f_c, f_t and G_f denote Young's modulus, Poisson's ratio, uniaxial compressive strength, uniaxial tensile strength and fracture energy, respectively.

A closed loop servo-controlled testing machine with a compression loading capacity of 250 kN was employed for loading the beam specimens in this study. For each specimen, a clip gauge was mounted on the bottom of the beam to measure the crack mouth opening displacement (CMOD). The tests were performed under CMOD control mode with a rate of 0.005mm/s.

2.2 Digital Image Correlation Technique and Determination of Opening/Sliding Displacements along the FPZ

Digital image correlation is an optical, non-contact measurement technique, which is usually

155 employed to analyze the displacement field on a specimen surface. By comparing images of
156 the specimen before and after deformation, the deformation of a specimen caused by the
157 applied load can be evaluated using the DIC technique. In this study, the camera was placed
158 perpendicular to the rock-concrete specimen side surface 1.5 m away. The speckled pattern
159 was made on the specimen surface using ordinary black spray paint. One digital image per
160 second was recorded using a digital camera with a resolution of 1024×768 pixels during
161 loading. Taking Specimen TPB30 as an example, a computational domain with 62×80 mm^2
162 was employed to cover its full ligament length. By picking up one out of each five pixels (1
163 pixel=0.0877 mm in this case), a computational grid of 22143 (121×183) points was selected
164 to conduct the deformation analysis in the X (perpendicular to the crack surface) and the Y
165 (parallel to the crack surface) directions (See Fig. 2). In Fig. 2, Line MN is just above the tip
166 of the pre-notch, and Lines M_1N_1, M_2N_2…M_nN_n (n=182) are parallel to Line MN with an
167 interval of 5 pixels. The opening displacement *u* along the X direction and sliding
168 displacement *v* along the Y direction corresponding to various loadings can be derived using
169 the DIC technique, which is elaborated as following:
170 Based on the *P-CMOD* curve of Specimen TPB30 (See Fig. 3) obtained from experiment,
171 Point P8, at the loading level of 5.5% of the post-peak load, is selected as an example to
172 elaborate how to derive the opening/sliding displacements. Fig. 4(a) and (b) illustrate the
173 deformation of line MN along the u and the v directions at Point P8, i.e., the opening and
174 sliding displacements at the tip of a notch. In Fig. 4(a), the opening displacements were
175 significantly increased in the 6-pixel points near the origin, which is caused by crack initiation.
176 Here, the points at the boundary of displacement jump are denoted as Points R and Q. By
177 calculating the distance between Points R and Q, the opening displacement 0.107 mm on
178 line MN is obtained. Correspondingly, the sliding displacement 0.0087 mm is derived based
179 on the experimental results. Then, the opening/sliding displacements on lines M_1N_1,

$M_2N_2…M_nN_n$ can be derived until both displacements reach zero, i.e. the crack tip is captured. Moreover, according to the obtained opening/sliding displacements in Fig. 4, the Points Q and R, which represent the deformation edges, can be used to define the crack profile on line MN corresponding to the loading Point P8. At that moment, the X-values of the profile on line MN correspond to the opening displacements of Points Q and R, respectively. Accordingly, the Y-values in Fig. 5 correspond to the sliding displacements of Points Q and R, respectively. Then, since the opening/sliding displacements on line MN are obtained at Point 8, the crack profile on line MN corresponding to Point 8 can be derived. Accordingly, the crack profile at Point 8 is obtained using the above-mentioned process by deriving the opening/sliding displacements on lines M_1N_1, $M_2N_2…M_nN_n$. In a similar manner, both the opening/sliding displacements and the crack profile can be obtained at any point of the P-CMOD curve. Therefore, the crack propagation and the FPZ evolution during the fracture process of the rock-concrete interface can be recorded using the DIC technique. To demonstrate, Fig. 5 illustrates the crack profile corresponding to Points P_2, P_4, and P_9, and the final failure image of the specimen TPB30.

3. Results and Discussions

3.1 Effects of Crack Length on Interface Mode Fracture Under TPB

Under TPB, due to the materials being asymmetric on both sides of a crack, the rock-concrete interface is a mixed mode fracture rather than a single mode opening fracture. Figs. 6 (a) to (j) illustrate crack evolution in Specimen TPB 30 with respect to points 1 to 10. In each figure, the opening displacement *u* and sliding displacement *v* along the crack are shown on both sides of the crack. It can be seen from these figures that, both the opening and sliding displacements increase almost linearly along the crack surface. Compared with the opening displacement, the sliding displacement is obviously smaller. For the purpose of

quantitative analysis, Fig. 7 presents the relationship of the ratio of v/u vs. the crack ratio a/D. Here, a is the overall crack length, which is the sum of the initial crack length and the crack propagation length. It can be seen from this figure that the ratios of v/u approximately showed a plateau when the crack tip was far from the free surface of the specimen, i.e. a/D is less than 0.6 in this study. Since v and u are caused by a bending moment and shear force, respectively, the ratio of v/u reflects the proportion of Modes II to I components, which has the similar physical meaning to the ratio of K_2/K_1. According to the result from literature [24], the ratio of K_2/K_1 also kept a plateau when there was no boundary effect at a rock-concrete interface. However, the ratio of v/u decreased rapidly when the crack tip was close to the free surface, i.e. a/D is close to 1, which may be attributed to the free surface effect. In the case of small size specimen in this study, the sliding displacement is 15% less than the opening displacement at the interfacial surface. It should be noted that the value of 15% is based only on the observation of this test, and more tests need to be carried out to get a sound conclusion.

3.2 FPZ Evolution at Rock-concrete Interface

According to the fictitious crack model proposed by Hillerborg [24], the tension-softening behaviors of the FPZ in cement-based materials can be described using the normal stress acting on the crack surface (σ) vs. crack opening displacement (w). In the relationship of σ-w, stress-free crack opening displacement w_0 is a significant parameter, which can determine the end of the FPZ. Taking the bilinear σ-w relationship of concrete [25] as an example, w_0 is set as $3.6G_f/f_t$. Thus, the FPZ length can be determined by the distance from the crack tip to the stress-free crack position. However, in the case of rock-concrete interface, the constitutive relationship of concrete was employed for describing the behavior of the rock-concrete interface as there is very limited reliable knowledge on the constitutive

relationship of rock-concrete interface from literature. Recently, aiming to understand the softening behavior of the rock-concrete interface, a bilinear σ-w relationship was determined by Dong et al. [26], and the relationship of $w_0 = 6G_f/f_t$ was proposed according to their research, which is also employed in this study. Based on the experimental results, f_t and G_f of the rock-concrete interface are 1.371 MPa and 19.3 N/m, respectively. Thus, w_0 is equal to 0.0844 mm.

When the initial crack tip opening displacement is less than w_0, no stress-free crack is formed so the FPZ length can be determined by positioning the crack tip. In comparison, when the displacement just reaches w_0, the FPZ is fully formed. Its length is 57.89 mm in this study, which is approximately corresponding to Point P7 (See Fig. 8). When the crack continuously propagates, the crack opening displacement keeps increasing, and the end of the FPZ will move forward and so will the crack tip. Therefore, according to the crack profile from experiment, the FPZ lengths can be derived, which are 41.44 and 24.69 mm with respect to Points P9 and P10 (See Fig. 8).

Fig. 9 illustrates the FPZ evolution during the fracture process in which $\triangle a$ denotes the crack propagation length. It can be seen that the FPZ length increases as the crack propagates until it has fully developed at Point A, which corresponds to the length of 60.09 mm. After that, the FPZ length decreases rapidly, showing the same variation trend as concrete [11]. The ratios are approximately 0.86 and 0.91 for the rock-concrete interface and concrete itself respectively, which are close to each other. After the development of a full FPZ, the effective crack consists of the newly formed stress-free crack, and the FPZ. If the ligament is long enough, the increase of newly formed crack is approximately equal to the increase of stress-free crack, so that the FPZ will keep a plateau. However, in the case of small-size specimens, the crack tip may be close to the specimen boundary when the FPZ fully develops. At that moment, the crack opening will increase sharply, which results in the

ending point of the FPZ moving forward rapidly. In this case, the increase of new crack initiation is less than the one of the new stress-free zone, resulting in the decrease of the FPZ length. It has been accepted that the boundary effect causes the decrease of the FPZ length in concrete [3]. Accordingly, the concept of local fracture energy was introduced based on the boundary effect model, and the bi-linear distribution of local fracture energy along the ligament was proposed [10]. Since the FPZ evolution of concrete and rock-concrete interface exhibited similar variation tendency, it may be concluded that the decrease of the FPZ length at the interface is caused by the boundary effect. The local fracture energy will decrease as well when the crack tip is close to the boundary. Certainly, it is worthy to conduct a study on the boundary effect at the rock-concrete interface in order to draw a sound conclusion.

3.3 Variation of FPZ Length in Rock-concrete Composite Specimens under TPB and FPS

In the case of the FPS series beams, the relationship of opening and sliding displacements on the crack surface is different from that of the TPB series beams discussed previously. It should be noted that the crack propagation at the post-peak load stage was not captured in the experiment due to the sudden break of FPS series specimens at the peak load. Meanwhile, although under FPS, the crack continuously propagates along the interface until reaching the top surface of the specimen for Specimens FPS 10-5-60, 4-15-30 and 4-10-20. For each FPS series specimen, four digital images were derived corresponding to different loads during the loading process from crack initiation to reaching peak load. In each image, the crack surface opening/sliding displacements can be derived through comparing with the reference image before loading. Together with the crack profiles, evolutions of the microcracks at the four selected loading moments are illustrated for each specimen in Figs.

10 to 12. The FPZ in the three specimens was not fully formed at the peak load since no stress-free cracks are formed at that moment. Meanwhile, there is a significant difference in the FPZ length of the TPB and the FPS series specimens at the peak load. The FPZ length is 7.89 mm for the Specimen TPB 30 while, for FPS specimens, the lengths are 36.84, 44.66 and 61.75 mm for FPS 10-5-60, 4-15-30 and 4-10-20, respectively. A natural rock surface obtained by fracturing a prismatic rock specimen by TPB was used for preparing the rock-concrete composite samples investigated in this study. Since there is no aggregate bridging mechanism at the rock-concrete interface, in the case of TPB, the rough surface only increases the contact area between rock and concrete, which improves the cohesive tension effect of the interface on a limited scale. However, in the case of FPS, the rough surface not only increases the contact area between the two materials but also increases the shear cohesive effect due to the interlocking from the naturally rough interface. Therefore, due to the existence of mode II component under FPS, the peak load significantly increases compared with under TPB. According to the experimental results, the peak load is 2.23 kN for Specimen TPB30. With respect to Specimens FPS 10-5-60, FPS 4-15-30 and FPS 4-10-20, the peak load are 18.84, 26.93 and 41.25 kN, respectively (See Table 1). It can be seen that with regards to the same size specimens (TPB30 and FPS 4-15-30), the peak load under FPS (Specimen FPS 4-15-30) is more than 10 times greater than the one under TPB (Specimen TPB30). From a qualitative estimation, the fracture energy at the peak load under FPS is far more than under TPB. From the viewpoint of the energy balance, the longer FPZ is needed, which can provide more tension and shear cohesive effects, to dissipate the fracture energy caused by the high peak load under FPS. This is why the FPZ length is

higher under FPS than under TPB as observed in this study. A longer FPZ provides a higher cohesive effect and increased cracking resistance. Therefore, if the linear elastic fracture mechanics is employed to predict the peak load of the interface, the underestimation of peak load on the fracture analysis of mixed mode dominant is more significant than the one of mode I dominant. Further, it is not appropriate to use linear elastic fracture mechanics to analyze mixed-mode fracture.

3.4 Variation of the Fracture Mode in Beams under FPS

According to the experimental setup shown in Fig. 1(b), the initial mode mixty ratio, K_2/K_1, before crack initiation can be derived as 0.595, 0.649 and 2.855 for specimens FPS 10-5-60, 4-15-30 and 4-10-20, respectively. Because no crack propagation occurs at that moment, linear elastic interfacial fracture mechanics can be employed to calculate the stress intensity factors (SIFs) at the tip of the pre-notch.

In the case of the FPS test of beams made of a single material, the crack will form and propagate perpendicular to the principle tensile stress. Therefore, even though a large ratio of K_{II}/K_I exists before crack initiation, the ratio will rapidly decrease after the crack is formed and the fracture mode will be dominated by Mode I [27]. The phenomenon can be explained by the fact that the crack usually propagates along the trajectory of the least cracking resistance. However, the scenario is different in the case of the rock-concrete interface. The crack propagation trajectory depends on the competition between the driving force and resistance with respect to the interface and the rock. It has been verified experimentally [28], that the crack can kink into rock even the interface is weaker than the rock (in this study, the initial fracture toughness' are 1.0 MPa·m$^{1/2}$ for rock vs. 0.2 MPa·m$^{1/2}$ for the interface). It

should be noted that, in the case of a crack kinking into the rock, the crack propagates perpendicular to the principal tensile stress. Therefore, it is similar to the mixed mode fracture of a single material in which the fracture mode will be dominated by Mode I as the crack propagates. In contrast, the fracture mode is still I-II mixed if the crack propagates along the interface. In this case, it is possible for the crack to kink into the rock after some propagation along the interface.

The relationship of v/u vs. a/D at Points P_1 to P_4 for each specimen is shown in Fig. 13. It is interesting to notice that the ratio of v/u remains almost constant for specimen FPS 4-10-20. It should also be noted that v and u can appropriately reflect the proportions of Modes II and I components, respectively, in the mixed mode fracture because they are caused by bending moment and shear force, respectively. From this point of view, the proportion of the mode II component in specimen FPS 4-10-20 does not decrease as the crack propagates as it does in concrete. Rather it keeps stable before the peak load is reached. Similarly, in the case of Specimen FPS 4-15-30, the ratio of v/u even slightly increases as the crack propagates before the peak load is reached. However, when a_0/D increases to 0.6, i.e. Specimen FPS 10-5-60, the scenario is different with the condition of a_0/D=0.2 and 0.3. At the early stage of crack propagation, i.e. Point P_1 of Specimen FPS 10-5-60, the ratio of v/u is 0.7. When the crack propagates from P_2 to P_4, the ratio decreases to around 0.2 and remains stable. It is worth pointing out that, the ratios of a_0/D corresponding to Points P_2 to P_4 exceed 0.9 at that moment, i.e. the specimen is almost broken even before the peak load is reached. It can be seen that the ratio of v/u changes as the crack propagates under a certain stress condition, e.g. Specimen FPS 10-5-60. Meanwhile, since the ratio of v/u reflects the proportion of

Modes II to I components, it has the similar physical meaning to the ratio of K_2/K_1. Therefore, it can be concluded that the ratio of K_2/K_1 will change as the crack propagates. Then, the initial mode mixty ratio, K_2/K_1, cannot reflect the proportion of variation in the Modes II and I components during crack propagation. Instead, the ratio of a/D has a significant effect on the fracture mode. In line with this, with the increase of Mode II component during a fracture process, the crack may divert into the rock after propagating a certain distance along the interface. Fig. 14 shows the failure mode of Specimen FPS 6-5-40, in which the crack propagated along the interface for about 25 mm, then diverted into the rock block. Moreover, the fracture mode will be dominated by Mode I when the ratio of a/D exceeds 0.9, i.e. the final fracture of the rock-concrete composite specimen is almost caused by bending. Therefore, in general, it is not reasonable to employ the initial mode mixty ratio to predict the crack trajectory, because the variation of K_2/K_1 is affected by the ratio of a/D as well. Particularly, in the case of a concrete dam with a crack along the interface between concrete and rock foundation, the mode mixty ratio with respect to crack initiation cannot be used to determine whether the crack will propagate along the interface or not. The ligament of the dam is long enough so that the crack may divert into the rock foundation and change the failure mode of the dam.

4. Conclusions

In this paper, the DIC technique is employed to investigate crack propagation at the rock-concrete interface under TPB and FPS. By deriving the opening/sliding displacement field of the crack surface, the FPZ evolution during a fracture process is discussed. Meanwhile, based on the variation of opening/sliding displacements under FPS, the fracture

mode during crack propagation is analyzed. According to the experimental study, the following conclusions can be drawn:

1. For the TPB series specimens, the interface FPZ length increases as a crack propagates until the full FPZ has developed, exhibiting the same variation trend as concrete. For the small size specimens in this study, the ratios of a/D corresponding to the total FPZ are 0.86 and 0.91 with respect to the rock-concrete interface and concrete itself, which showed the similar boundary effects.
2. There is a very short FPZ (7.89 mm) at the peak load under TPB, while the FPZ reaches 36.84, 44.66 and 61.75 mm long under FPS with a_0/D=0.6, 0.3 and 0.2, respectively. Therefore, the short FPZ length results in the less nonlinear fracture characteristic of rock-concrete interface with Mode I dominant fracture, while the nonlinear fracture characteristic is more significant for mixed mode fracture of the rock-concrete interface.
3. The fracture mode varies as the crack propagates in the following manner: for the TPB series specimens, the ratio of u/v at the tip of the notch of the interface remains at a plateau until the crack tip is close to the specimen boundary. For the FPS series specimens with a small a_0/D (i.e. $a_0/D \leq 0.4$), the Mode II component may increase as the crack propagates, resulting in the crack diverting into the rock. Finally for the FPS series specimens with large a_0/D (i.e. $a_0/D \geq 0.6$), the fracture mode rapidly falls into Mode I until the beam is broken into two halves.

Acknowledgement

The financial support of the National Natural Science Foundation of China under the grants of NSFC 51478084, NSFC 51421064 and NSFC 51109026, and partial financial support from the UK Royal Academy of Engineering through the Distinguished Visiting Fellow Scheme under the grant DVF1617_5_21 is gratefully acknowledged.

References

[1] Sujatha V, Kishen JMC. Energy release rate due to friction at bimaterial interface in dams. J Eng Mech. 2003;129:793-800.

[2] Yang S, Song LI, Li ZHE, Huang S. Experimental investigation on fracture toughness of interface crack for rock/concrete. Int J Mod Phys B. 2008;22:6141-8.

[3] Wittmann FH, Hu XZ. Fracture process zone in cementitious materials. Int J Fracture. 1991;51:3-18.

[4] Hu XZ. An asymptotic approach to size effect on fracture toughness and fracture energy of composites. Eng Fract Mech. 2002;69:555-64.

[5] Červenka J, Chandra Kishen JM, Saouma VE. Mixed mode fracture of cementitious bimaterial interfaces: Part II: numerical simulation. Eng Fract Mech. 1998;60:95-107.

[6] Otsuka K, Date H. Fracture process zone in concrete tension specimen. Eng Fract Mech. 2000;65:111-31.

[7] Cotterell B, Mai Y-W. Crack growth resistance curve and size effect in the fracture of cement paste. J Mar Sci. 1987;22:2734-8.

[8] Hu XZ, Wittmann F. Size effect on toughness induced by crack close to free surface. Eng Fract Mech. 2000;65:209-21.

[9] Hu XZ, Wittmann FH. An analytical method to determine the bridging stress transferred within the fracture process zone: II, Application to mortar. Cem Concr Res. 1992;22:559-70.

[10] Duan K, Hu XZ, Wittmann FH. Boundary effect on concrete fracture and non-constant fracture energy distribution. Eng Fract Mech. 2003;70:2257-68.

417 [11] Wu Z, Rong H, Zheng J, Xu F, Dong W. An experimental investigation on the FPZ
418 properties in concrete using digital image correlation technique. Eng Fract Mech.
419 2011;78:2978-90.
420 [12] Dong W, Zhou X, Wu Z. On fracture process zone and crack extension resistance of
421 concrete based on initial fracture toughness. Constr Build Mater. 2013;49:352-63.
422 [13] Lin Q, Yuan H, Biolzi L, Labuz JF. Opening and mixed mode fracture processes in a
423 quasi-brittle material via digital imaging. Eng Fract Mech. 2014;131:176-93.
424 [14] Alberto A, Valente S. Asymptotic fields at the tip of a cohesive frictional crack growing at
425 the bi-material interface between a dam and the foundation rock. Eng Fract Mech.
426 2013;108:152-61.
427 [15] Barpi F, Valente S. The cohesive frictional crack model applied to the analysis of the
428 dam-foundation joint. Eng Fract Mech. 2010;77:2182-91.
429 [16] Zhong H, Ooi ET, Song C, Ding T, Lin G, Li H. Experimental and numerical study of the
430 dependency of interface fracture in concrete–rock specimens on mode mixity. Eng Fract
431 Mech. 2014;124-125:287-309.
432 [17] Mahal M, Blanksvärd T, Täljsten B, Sas G. Using digital image correlation to evaluate
433 fatigue behavior of strengthened reinforced concrete beams. Eng Struct. 2015;105:277-88.
434 [18] Alam SY, Saliba J, Loukili A. Fracture examination in concrete through combined digital
435 image correlation and acoustic emission techniques. Constr Build Mater. 2014;69:232-42.
436 [19] Enfedaque A, Gálvez JC, Suárez F. Analysis of fracture tests of glass fibre reinforced
437 cement (GRC) using digital image correlation. Constr Build Mater. 2015;75:472-87.
438 [20] Trivedi N, Singh RK, Chattopadhyay J. Investigation on fracture parameters of concrete

through optical crack profile and size effect studies. Eng Fract Mech. 2015;147:119-39.

[21] Shah SG, Kishen JMC. Fracture properties of concrete-concrete interfaces using digital image correlation. Exp Mech. 2011;51:303-13.

[22] Corr D, Accardi M, Graham-Brady L, Shah S. Digital image correlation analysis of interfacial debonding properties and fracture behavior in concrete. Eng Fract Mech. 2007;74:109-21.

[23] Nagashima T, Omoto Y, Tani S. Stress intensity factor analysis of interface cracks using X-FEM. Int J Numer Meth Eng. 2003;56:1151-73.

[24] Hillerborg A, Modéer M, Petersson PE. Analysis of crack formation and crack growth in concrete by means of fracture mechanics and finite elements. Cem Concr Res. 1976;6:773-81.

[25] Petersson PE. Crack growth and development of fracture zones in plain concrete and similar materials. Division of Building Materials, Lund Institute of Technology, Report TVBM-1006, Sweden, 1981.

[26] Dong W, Wu Z, Zhou X. Fracture mechanisms of rock-concrete interface: experimental and numerical. J Eng Mech, ASCE. 2016;142:04016040.

[27] Wu Z, Rong H, Zheng J, Dong W. Numerical method for mixed mode I–II crack propagation in concrete. J Eng Mech, ASCE. 2013;139:1530-8.

[28] Slowik V, Chandra Kishen JM, Saouma VE. Mixed mode fracture of cementitious bimaterial interfaces;: Part I: Experimental results. Eng Fract Mech. 1998;60:83-94.

Appendix I Table

Table 1. Specimen Geometries and Experimental Results

Name of specimens	$L \times D \times B$ (mm^3)	a_0 (mm)	C_1 (mm)	L_1：L_2	P_{max} (kN)	K_2/K_1
TPB30		30	-	-	2.23	-
FPS 4-10-20		20	10	4	41.25	0.595
FPS 4-15-30	500×100×100	30	15	4	26.93	0.649
FPS 10-5-60		60	5	10	18.84	2.855
FPS 6-5-40		40	5	6	32.97	3.740

Table 2. Materials Properties of Concrete, Rock and Interface

Materials	Density (kg/m^3)	E_t (GPa)	v	f_c (MPa)	f_t (MPa)	G_f (N/m)
Concrete	2400	30.26	0.24	36.1	2.88	87
Rock	2668	64.39	0.20	119.2	8.65	119.7
Interface	—	—	—	—	1.37	19.3

Captions of figures

Fig. 1. Experimental setup: (a) Three-point bending test; and (b) Four-point shearing test

Fig. 2. Computational domains of Specimen TPB 30

Fig. 3. *P-CMOD* curve of Specimen TPB 30

Fig. 4. Displacement along Line MN on Specimen TPB 30: (a) Crack tip opening displacement of Point P8; and (b) Crack tip sliding displacement of Point P8

Fig. 5. Crack profiles of Specimen TPB 30 and final failure mode

Fig. 6. Evolution of the microcrack of Specimen TPB 30: (a) P_1=78%P_{max} (pre-peak); (b) P_2=P_{max}; (c) P_3=83.03%P_{max} (post-peak); (d) P_4=49.3%P_{max} (post-peak); (e) P_5=32%P_{max} (post-peak); (f) P_6=15.5%P_{max} (post-peak); P_7=11%P_{max} (post-peak); (h) P_8=5.5%P_{max} (post-peak); and (i) P_9=3.18%P_{max} (post-peak)

Fig. 7. Relationship of *v*/*u* vs. *a*/D in three-point bending beam

Fig. 8. FPZ evolution after the initiation of a full FPZ

Fig. 9. FPZ evolution in Specimen TPB 30

Fig. 10. Evolution of the microcrack in Specimen FPS 10-5-60: (a) P_1=63.1%P_{max}; (b) P_2=76.5%P_{max}; (c) P_3=82.6%P_{max}; and (d) P_4=98.3%P_{max}

Fig. 11. Evolution of the microcrack in Specimen 4-15-30: (a) P_1=65.1%P_{max}; (b) P_2=84.8%P_{max}; (c) P_3=95.9%P_{max}; and (d) P_4=97%P_{max}

Fig. 12. Evolution of the microcrack in Specimen FPS 4-10-20: (a) P_1=74.8%P_{max}; (b) P_2=90.9%P_{max}; (c) P_3=96.3%P_{max}; and (d) P_4=98.2%P_{max}

Fig. 13. Relationship of *v*/*u* vs. *a*/*D* for FPS beams

Fig. 14. Failure mode of Specimen FPS 6-5-40

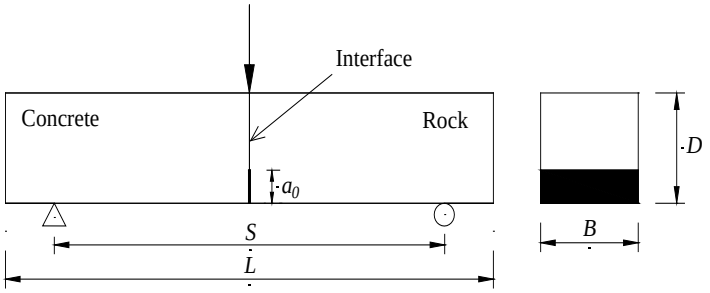

(a) Three-point bending test

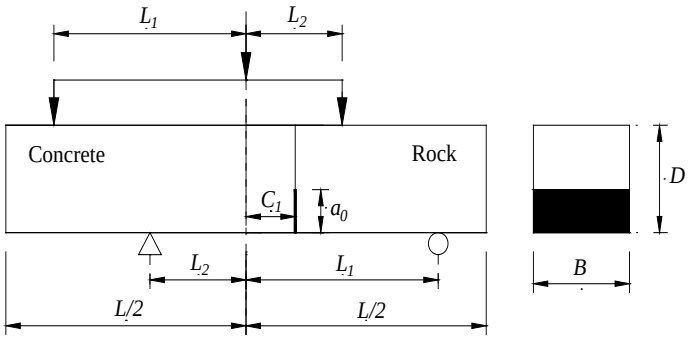

(b) Four-point shearing test

Fig. 1. Experimental setup

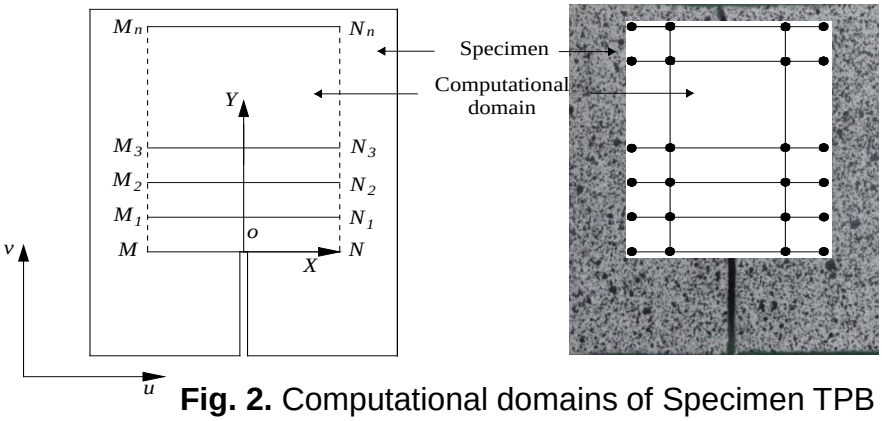

Fig. 2. Computational domains of Specimen TPB 30

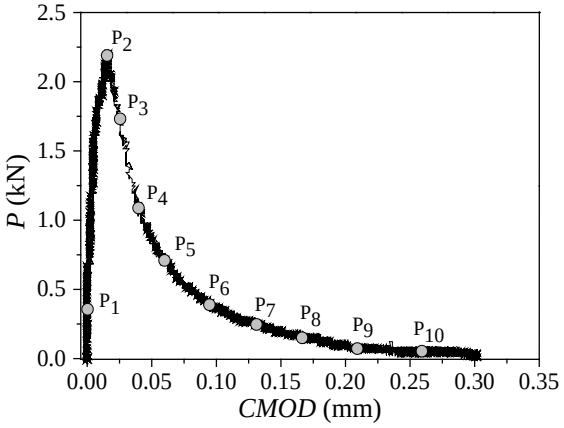

Fig. 3. *P-CMOD* curve of Specimen TPB 30

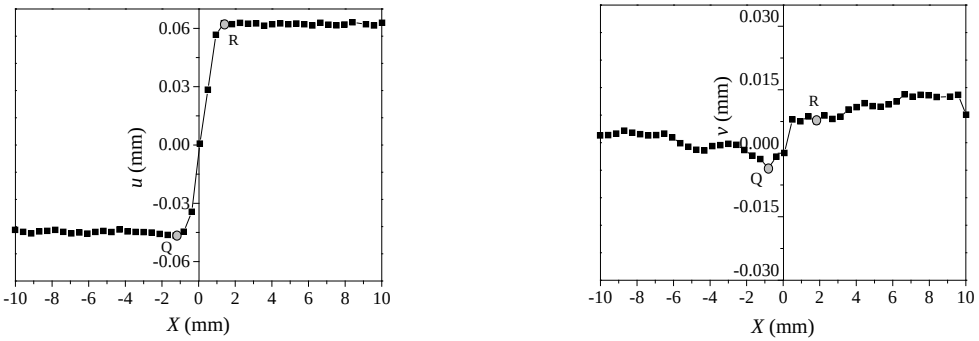

(a) Crack tip opening displacement of Point P8 (b) Crack tip sliding displacement of Point P8

Fig. 4. Displacement along Line MN on Specimen TPB 30

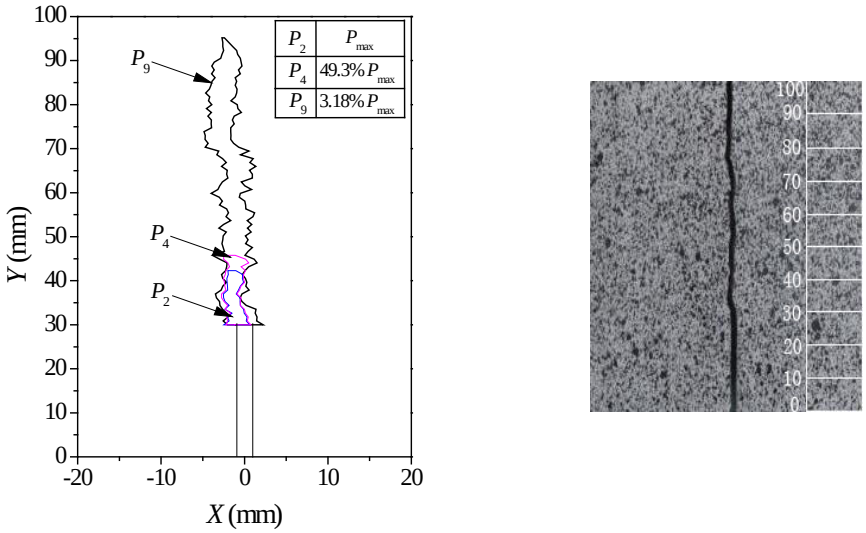

(a) Crack profiles at Points P_2, P_4 and P_9 (b) Failure mode

Fig. 5. Crack profiles of Specimen TPB 30 and final failure mode

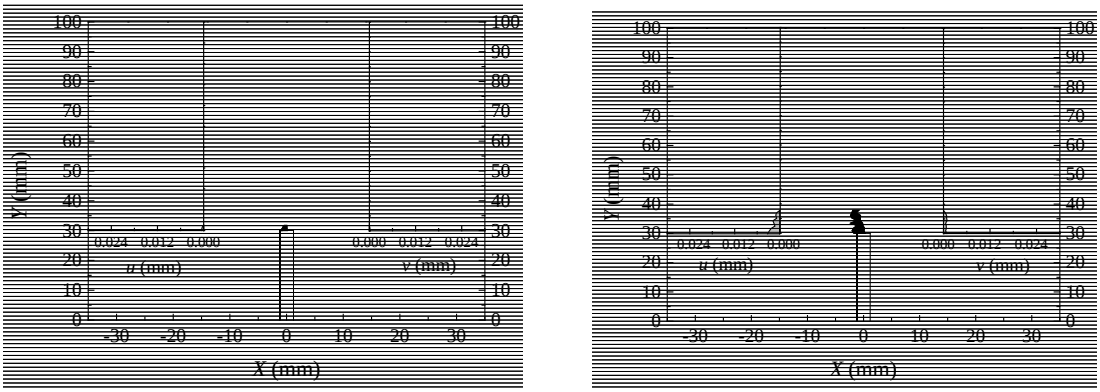

(a) P_1=15.5%P_{max} (pre-peak) (b) P_2=P_{max}

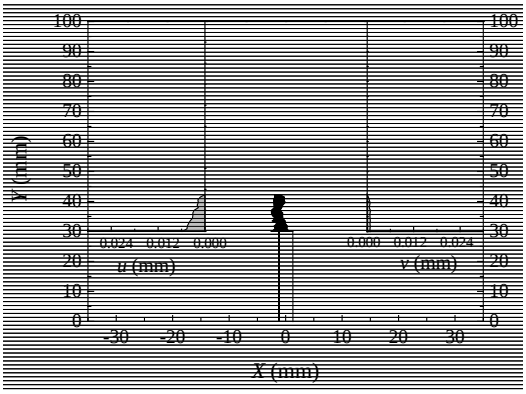

(c) P_3=83.03%P_{max} (post-peak)

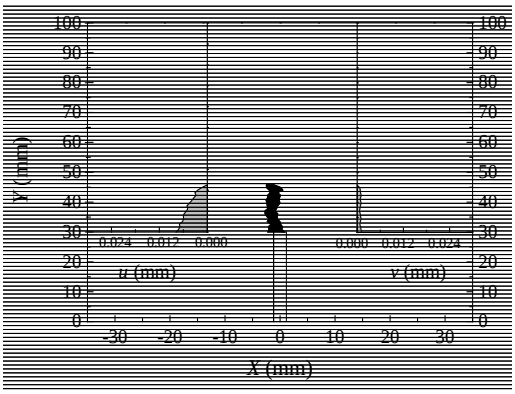

(d) P_4=49.3%P_{max} (post-peak)

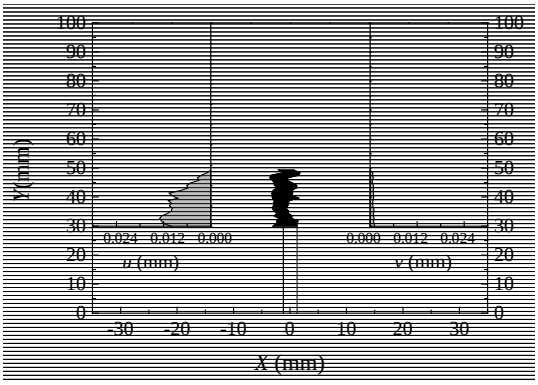

(e) P_5=32%P_{max} (post-peak)

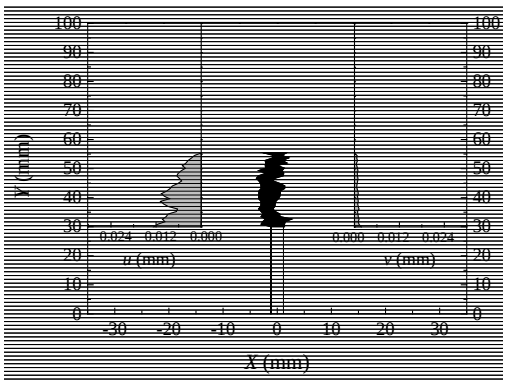

(f) P_6=15.5%P_{max} (post-peak)

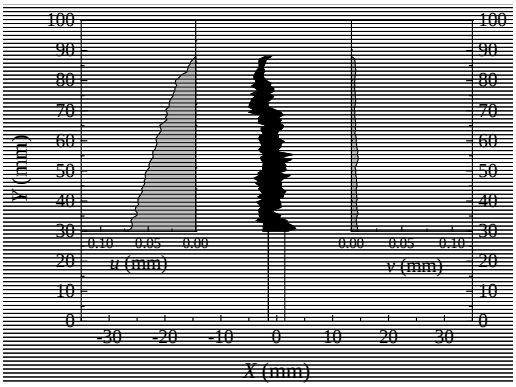

(g) P_7=11%P_{max} (post-peak)

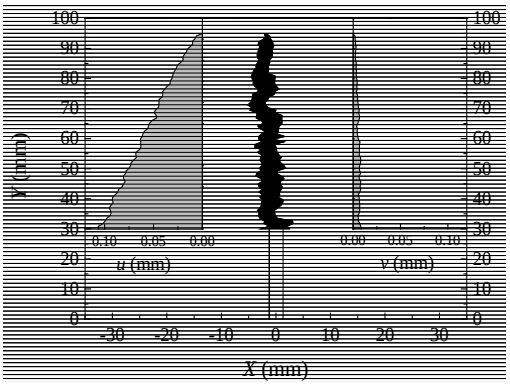

(h) P_8=5.5%P_{max} (post-peak)

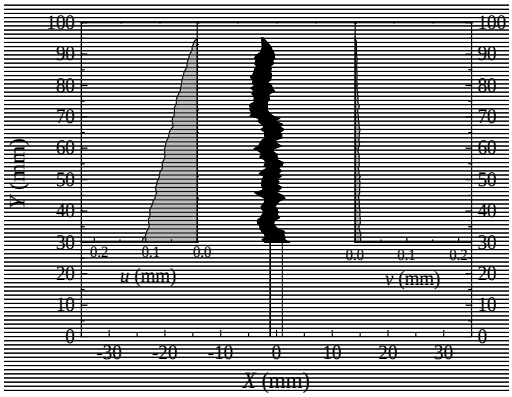

(i) P_9=3.18%P_{max} (post-peak)

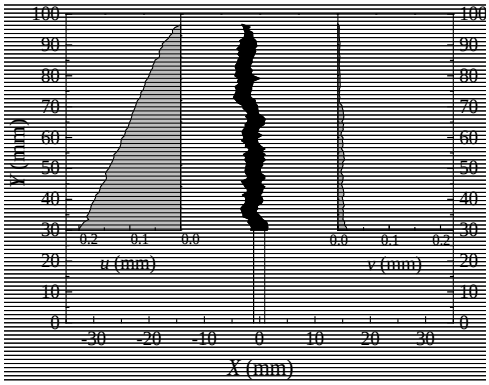

(j) P_{10}=2.2%P_{max} (post-peak)

Fig. 6. Evolution of microcrack of Specimen TPB 30

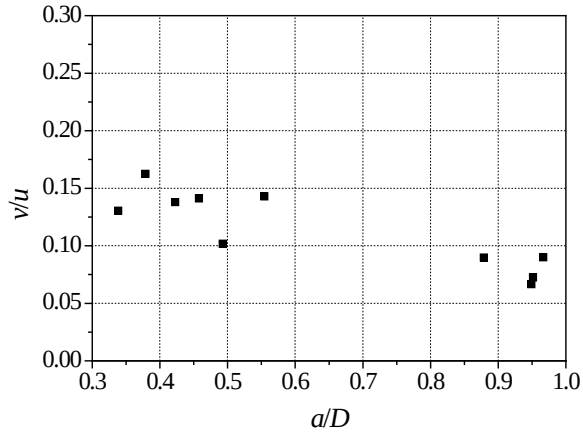

Fig. 7. Relationship of *v*/*u* vs. *a*/*D* in three-point bending beams

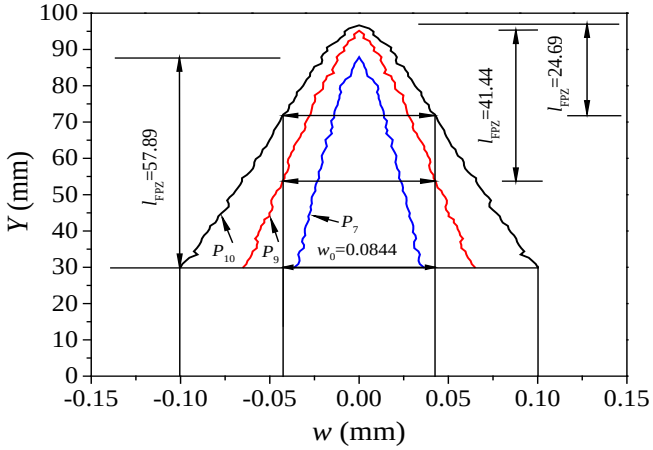

Fig. 8. FPZ evolution after the initiation of a full FPZ

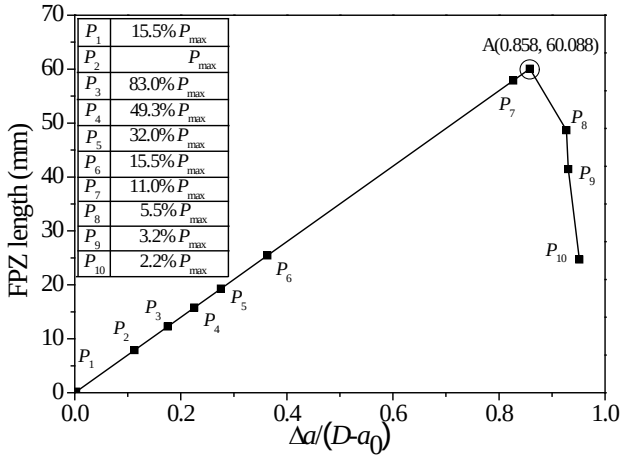

Fig. 9. FPZ evolution in Specimen TPB 30

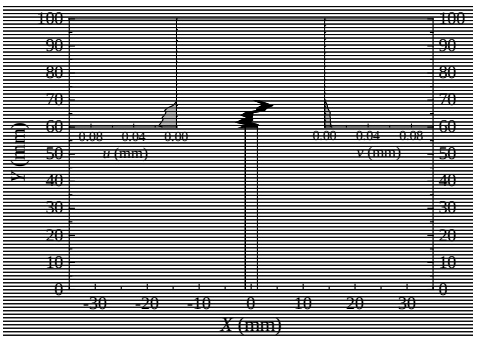

(a) P_1=63.1%P_{max}

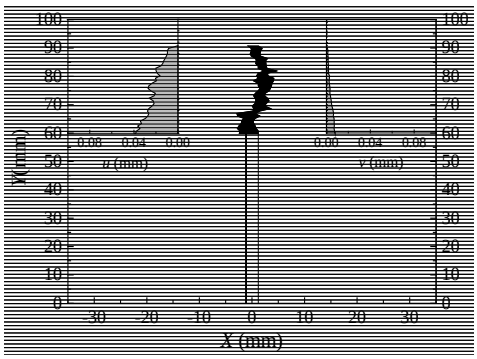

(b) P_2=76.5%P_{max}

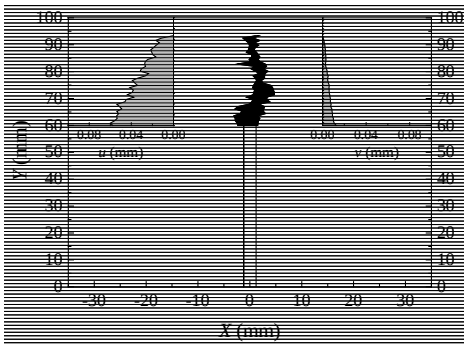

(c) P_3=82.6%P_{max}

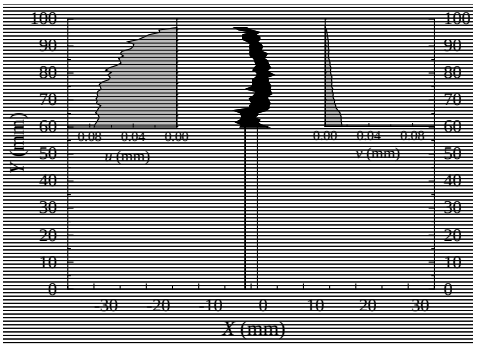

(d) P_4=P_{max}

Fig. 10. Evolution of the microcrack in Specimen FPS 10-5-60

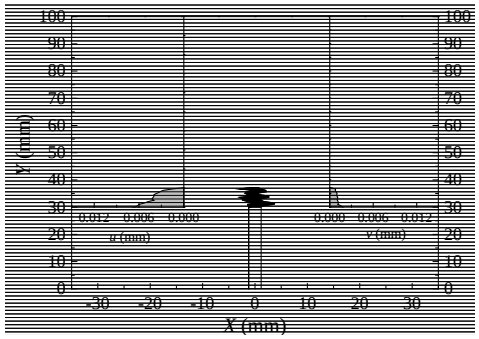

(a) P_1=65.1%P_{max}

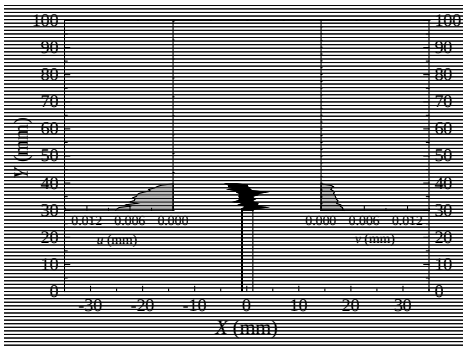

(b) P_2=84.8%P_{max}

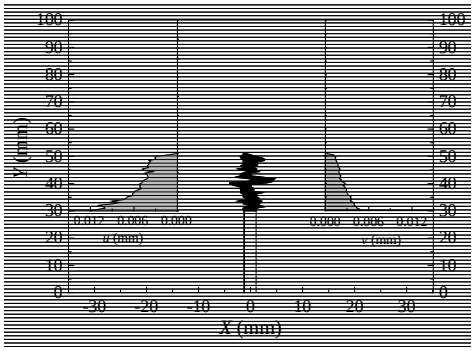

(c) P_3=95.9%P_{max}

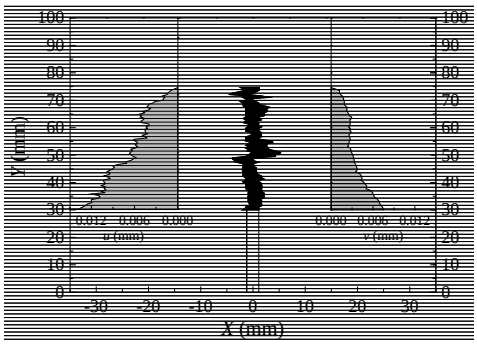

(d) P_4=P_{max}

Fig. 11. Evolution of the microcrack in Specimen 4-15-30

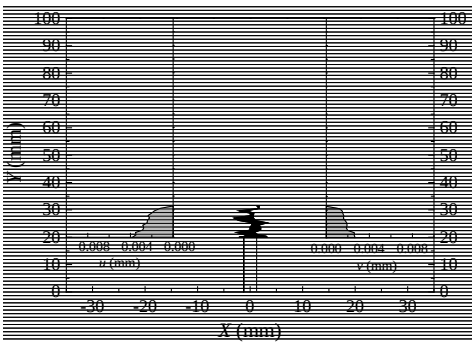

(a) P_1=74.79%P_{max}

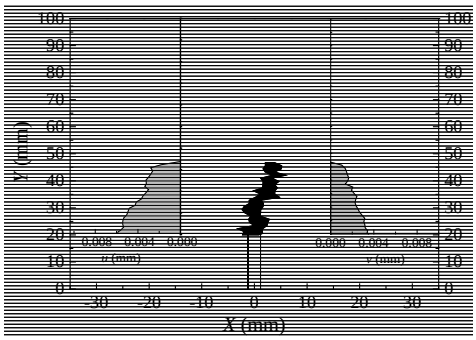

(b) P_2=90.9%P_{max}

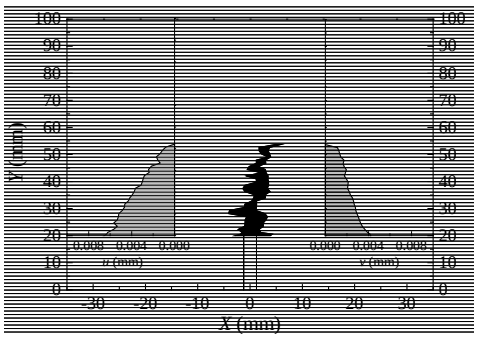

(c) P_3=96.25%P_{max}

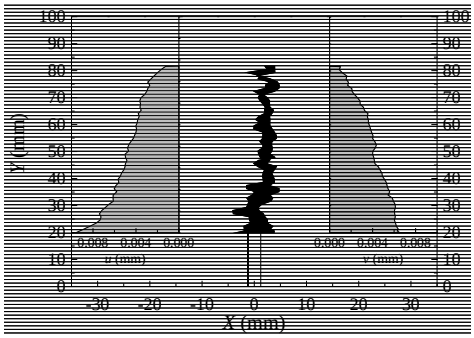

(d) P_4=P_{max}

Fig. 12. Evolution of the microcrack in Specimen FPS 4-10-20

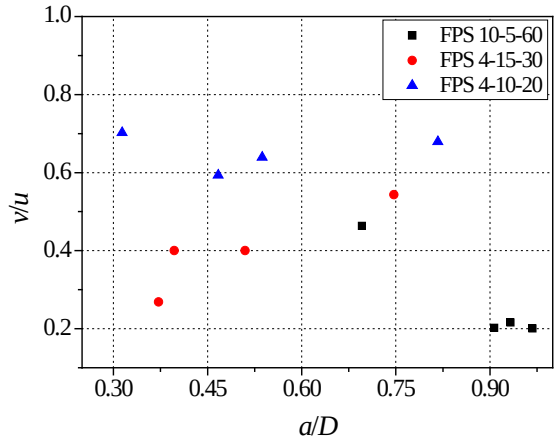

Fig. 13. Relationship of *v*/*u* vs. *a*/*D* for FPS beams

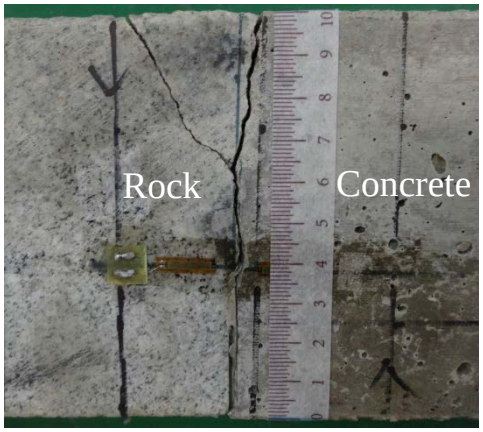

Fig. 14. Failure mode of Specimen FPS 6-5-40